P. I. B. International Journal of Applied Pharmaceutics

ISSN- 0975-7058 Vol 18, Issue 3, 2026

Original Article

UNVEILING THE INTERACTION OF ANDROGRAPHOLIDE WITH CATALASE: A COMBINED COMPUTATIONAL AND EXPERIMENTAL STUDY

PUTU INDAH BUDI APSARI[1,2*], DEWA AYU AGUS SRI LAKSEMI[3], BAGUS KOMANG SATRIYASA[4], I. KETUT SURYANA[5], DYAH KANYA WATI[6], I. MADE AGUS GELGEL WIRASUTA[7]

[1]Faculty of Medicine, Udayana University, Denpasar, Bali, Indonesia. [2]Microbiology and Parasitology Department, Faculty of Medicine and Health Sciences, Warmadewa University, Denpasar, Bali, Indonesia. [3]Department of Parasitology, Faculty of Medicine Universitas Udayana, Denpasar, Bali, Indonesia. [4]Department of Pharmacology, Faculty of Medicine, Udayana University, Denpasar, Bali, Indonesia. [5]Internal Medicine Department, Prof. Ngoerah Hospital, Denpasar, Bali, Indonesia. [6]Child Health Department, Prof. Ngoerah Hospital Denpasar, Denpasar, Bali, Indonesia

[*]Corresponding author: Putu Indah Budi Apsari; [*]Email: putuindah51@yahoo.com

Received: 14 Jan 2026, Revised and Accepted: 10 Mar 2026

ABSTRACT

Objective: This study investigated the effect of andrographolide, alone and in combination with artesunate, on hepatic catalase expression in a murine malaria model and evaluated its molecular interaction with catalase using computational approaches.

Methods: Molecular docking and molecular dynamics simulations have been performed to assess interactions between andrographolide, its derivatives, phase I and II metabolites with human erythrocyte catalase (PDB ID: 1DGF). *In vivo* experiments used *Mus musculus*Balb/C infected with *Plasmodium berghei* ANKA (PbA) and treated with artesunate (2.4 mg/kg), andrographolide (50 mg/kg), and their combination. Hepatic catalase expression was quantified by immunohistochemistry and ImageJ-based analysis. Statistical analysis was performed using one-way ANOVA followed by Tukey's post-hoc test, with a significance level set at $p<0.05$.

Results: Docking revealed strong binding of andrographolide metabolites to catalase (binding energy range −6.4 to −9.9 kcal/mol), exceeding that of artemisinin (−7.1 kcal/mol). Molecular dynamics showed stable complexes, with andrographolide inducing adaptive conformational changes. *In vivo*, catalase expression was significantly elevated in infected untreated mice but was reduced in treated groups. Notably, combination therapy reduced catalase expression to levels statistically indistinguishable from uninfected controls.

Conclusion: Andrographolide and its metabolites strongly interact with catalase in silico and modulate hepatic catalase expression *in vivo*, supporting its role as an adjuvant antioxidant strategy in malaria.

Keywords: Andrographolide, Catalase, Malaria, Molecular docking, Molecular dynamics

DOI: https://dx.doi.org/10.22159/ijap.2026v18i3.58100 Journal homepage: https://innovareacademics.in/journals/index.php/ijap

INTRODUCTION

Malaria, caused by *Plasmodium spp*. and transmitted by female Anopheles mosquitoes, remains a major global health challenge. In 2023, an estimated 263 million cases and 597,000 deaths were reported worldwide [1]. Indonesia has the second highest number of malaria cases in Asia after India [2]. In 2023, malaria cases in Indonesia reached 418,546 cases. Artemisinin-based combination therapies (ACTs), recommended by WHO for the treatment of uncomplicated malaria, have been an integral part of the remarkable successes in global malaria control seen over the last 20 years and found to be resistance in some region [1]. Artemisinin resistance by *Plasmodium spp.* is a major problem in malaria eradication in worldwide and Indonesia that threatens the sustainability of global efforts to reduce the burden of malaria [3]. Mechanisms contributing to malaria resistance is oxidative stress. Oxidative stress plays a dual role in malaria pathogenesis. Reactive oxygen species (ROS) generated by both the parasite and host immune response contribute to parasite killing but can also damage host tissues. Antioxidant enzymes such as superoxide dismutase and catalase are therefore critically involved in maintaining redox balance during infection. Dysregulation of these enzymes has been linked to disease severity and treatment response. *Andrographis paniculata* (sambiloto) has been traditionally used as an antimalarial agent and is known to possess anti-inflammatory and antioxidant properties [4]. Andrographolide, its major diterpenoid constituent, has demonstrated anti-plasmodial activity and the ability to modulate oxidative stress pathways. However, direct evidence regarding its effect on catalase expression in hepatic malaria, particularly under artemisinin-based combination therapy, remains limited [5, 6]. This study integrates in silico and *in vivo* approaches to evaluate the interaction of andrographolide, its derivatives, and metabolites with catalase and to assess their effect on hepatic catalase expression in a malaria murine model.

MATERIALS AND METHODS

Molecular docking

Molecular docking was performed using hardware consisting of an Asus Intel Core i5, 4 GB RAM, Autodock 4.2.6 (https://autodock.scripps.edu/wp-content/uploads/sites/56/2021/10/autodocksuite-4.2.6.i86Windows.exe), MGLtools 1.5.7 (https://ccsb.scripps.edu/download/262/), Open Babel 3.1.1 (https://github.com/openbabel/openbabel/releases/tag/openbabel-3-1-1), and BIOVIA Discovery Studio (https://discover.3ds.com/discovery-studio-visualizer-download) software. The three-dimensional structure of human erythrocyte catalase (PDB ID: 1DGF) was obtained from the RCSB Protein Data Bank. Protein preparation, including chain selection and removal of the native ligand (protoporphyrin IX), was performed using UCSF Chimera v1.19 and BIOVIA Discovery Studio. Redocking validation using AutoDock4 yielded an RMSD of 0.403 Å, confirming protocol's reliability. Binding energies and inhibition constants were calculated using AutoDock Tools. Docking results were visualized and interaction types analyzed using BIOVIA Discovery Studio [7]. The selected chains were validated using the Autodock4 and Autogrid4 programs by redocking the chains with their native ligands. An RMSD reference of less than 3 Amstrong was considered valid and could be used as a docking receptor with the test compound. ChainD selected to use as protein chain validation. Validation run in Autodock4 reveal Ki 3.49 fM (femtomolar), Native Ligand was Protoporphyrin IX Containing Fe with RMSD (Å) 0.403, binding energy was-19.72(kcal/mol), Grid Points were x: 32.317, y: 51.325, z: 26.072. The docking results are then visualized using BIOVIA Discovery Studio and analyzed for the types of bonds and amino

acid residues formed. This simulation provides insight into the stability of the complex through the free energy (binding free energy) which is said to be good or strong when less than-6 kcal/mol [8]. Parent compound (andrographolide), derivates (deoxyandrographolide, neoandrographolide), metabolite phase I(14 deoxy-11, 12 dehydroandrografolid, isoandrographolide, 14-deoxy-12-hydroxy-andrographolide, 14-deoxyandrographolide, 3-oxoandrographolide) were accessed from Pubchem. Metabolite phase II of andrographolide: andrographolide-19-o-beta-d-glucuronide (m1), isoandrographolide-19-o-beta-d-glucuronide (m2), 14-deoxy-12-hydroxyandrographolide-19-o-beta-d-glucuronide (m3),andrographolide-19-o-[6'-methyl-beta-d-glucuronide] (m4), 14-deoxy-12(13)-en-andrographolide-19-o-beta-d-glucuronide (m5), 14-deoxyandrographolide-19-o-beta-d-glucuronide (m6),3-oxoandrographolide-19-o-beta-d-glucuronide (m7)structure from previous research [9] were first saved in an image format (PNG) and uploaded to the Optical Structure Recognition Application (OSRA) via https://cactus.nci.nih.gov/cgi-bin/osra/index.cgi. After the file was selected and submitted, the system extracted the chemical structure and generated its SMILES representation. The SMILES code was then translated using the translate SMILES feature to obtain the molecular structure in three-dimensional format. The resulting 3D structure was subsequently converted into Protein Data Bank (. pdb) format by selecting the PDB and 3D options and downloaded. The generated. pdb file was visualized using the RCSB PDB 3D Viewer by opening the file and applying the structural display, yielding a three-dimensional molecular representation suitable for further analysis. All compound used as ligand tested with target IDGF. The prediction of the Rule of Five for each ligand was performed by copying the ligand SMILES from PubChem (https://pubchem.ncbi.nlm.nih.gov/compound), followed by running ADMET prediction using the pkCSM (https://biosig.lab.uq.edu.au/pkcsm/prediction_single) web server. The Rule of Five components that appear include molecular weight (Da), LogP, number of rotatable bonds, number of hydrogen bond acceptors, number of hydrogen bond donors, and surface area [10].

Molecular dynamic

The molecular dynamics simulation was performed using a Victus by HP Gaming workstation equipped with a 13th Gen Intel® Core™ i7-13700HX processor (24 CPUs) with a speed ofapproximately 2.1 GHz, 32 GB of memory, and an NVIDIA GeForce RTX 4060 laptop GPU with 8 GB VRAM. Modeling and simulation were conducted using GROMACS version 2025.3. (patch release notes-12 September 2025). System preparation began with ligand preprocessing in BIOVIA Discovery Studio by adding hydrogen atoms, while protein preparation was carried out using the Dock Prep feature in Chimera v1.19, including hydrogen addition and charge assignment [11]. Ligand topology was generated and parameterized using swissparam.ch with the CHARMM36 force field. The protein was parameterized using the CHARMM36 force field, consistent with the ligand parameters generated by SwissParam, which by default provides ligand topologies/parameters compatible with CHARMM36. This is verified in topol. top by the inclusion of the CHARMM36 force-field files (#include "charmm36.ff/forcefield.itp"). The system was then placed in a cubic simulation box and solvated using the Transferable Intermolecular Potential with 3 Points (TIP3P) water model. Ionization was performed by adding Na^+ and Cl^- ions to reach a final concentration of 0.15 mol/l while neutralizing the total system charge. The solvated protein–ligand complex was first energy-minimized to remove unfavorable contacts and relax the system prior to dynamics. The minimized structure was then equilibrated in the Number of particles, Volume, and Temperature (NVT) ensemble with positional restraints on the solute (protein and ligand) to allow the solvent and ions to reorganize around the complex while maintaining its initial conformation; the temperature was maintained at 300 K using the velocity-rescale thermostat, with separate temperature coupling for the solute and for the solvent. Equilibration was subsequently continued in the number of particles, Pressure, and Temperature (NPT) ensemble to stabilize the system density at 1 bar; pressure was regulated isotopically using the Parrinello–Rahman barostat, and the temperature was maintained at 300 K using the same thermostat scheme, with positional restraints released prior to the production phase. Production molecular dynamics was then carried out for 100 ns under NPT conditions using a 2fs integration time step, starting from the final equilibrated state without reassigning velocities. Bonds involving hydrogen were constrained to enable the chosen time step, long-range electrostatics were treated using the particle-mesh Ewald method, and nonbonded interactions were evaluated with a 1.2 nm cutoff and smooth switching for van der Waals interactions. Periodic boundary conditions were applied in all directions, and system coordinates, energies, and log information were saved every 10 ps [12]

Production simulations were carried out using the leap-frog integrator with a time step of 2 femtoseconds for 50 ns for each system. Structural snapshots were recorded every 0.01 ns, yielding a total of 5000 frames used for thermodynamic analyses [13]. The analyzed parameters included Root mean Square Deviation (RMSD) to assess structural stability and protein–ligand interactions, Root mean Square Fluctuation (RMSF) to examine C-alpha residue flexibility, the number of hydrogen bonds as an indicator of complex stability, Radius of Gyration (Rg) to evaluate protein compactness, and Solvent Accessible Surface Area (SASA) to determine the solvent-exposed surface area of the protein. Visualization and post-simulation processing were performed using OriginPro 2024 [14].

Extraction of *Andrographis paniculata* herb

Sambiloto was collected from Girimulyo Village, Nanggulan District, KulonProgo Regency, Yogyakarta, Indonesia (ordinate point:-7.728283475098428, 110.15053712340968). The plant material was taxonomically identified and authenticated by a botanist at the Pharmaceutical Biology Laboratory, Faculty of Pharmacy, Gadjah Mada University, Indonesia, and a voucher specimen (No. BF/143/Ident/Det/VII) was deposited for reference. A total of 1 kg of *Andrographis paniculata* herbal simplicia was soaked in hot water until softened, then steamed for 30 min and ground to reduce particle size. The simplicia was macerated for 24 h using 5 l of a solvent mixture consisting of 96% ethanol and 0.5% acetic acid in an 85:15 (v/v) ratio. After maceration, the macerate was separated from the residue. The residue was subsequently remacerated three times using the same procedure and solvent system. All macerates were concentrated using a rotary vacuum evaporator to obtain viscous extracts. The extraction yields of the maceration and each remaceration stage were calculated. The maceration solvent was prepared by mixing 4.25 l of 96% ethanol with 750 ml of 0.5% acetic acid solution, which was prepared from glacial acetic acid through serial dilution with distilled water [15].

Extract characterization

The moisture content of the extract was determined using the gravimetric method by drying the sample at 105 °C until a constant weight was achieved. The pH of the extract was measured using a calibrated pH meter with standard buffer solutions of pH 4.0, 7.0, and 10.0. Prior to measurement, 1 g of the extract was diluted with 10 ml of distilled water [16].

Crystallization and recrystallization of andrographolide

The viscous extracts obtained from maceration and first remaceration were repeatedly washed with ethyl acetate until the filtrate became clear, followed by drying at 50 °C. The extract was then dissolved in hot methanol (80 °C) and filtered while hot. The filtrate was stored in a freezer for 24 h and subsequently allowed to stand at room temperature for 3–5 days until crystal formation occurred. Recrystallization was performed using cold methanol. The resulting white andrographolide crystals were dried at 50 °C [17].

Preparation of andrographolide suspension

A total of 50 mg of andrographolide was accurately weighed and combined with 200 mg of propylene glycol, 200 mg of Tween 80, and 1 ml of distilled water. The mixture was homogenized using a vortex mixer until a uniform andrographolide suspension was obtained.

Animal procedure

A completely randomized post-test only group design was employed using 25 male BALB/c *Mus musculus* aged 7–8 w with body weights ranging from 25–30 g, following a 1-week acclimatization period. Animals were housed at a room temperature of 25 °C with a 12 h light–dark cycle, provided with standard Turbo pellet feed and water ad libitum, and kept in cages measuring 40 × 50 cm, with five mice per cage for each group [18]. The mice were divided into five groups: uninfected group as normal control, a negative control group receiving no treatment; a positive control group treated with artesunate (Artesun for injection, Guilin Pharmaceutical Co., LTD, P. R. China) at a dose of 2.4 mg/kg body weight administered intraperitoneally; treatment group 1 receiving andrographolide at 50 mg/kg body weight administered orally; and treatment group 2 receiving a combination of artesunate (2.4 mg/kg body weight, intraperitoneally) and andrographolide (50 mg/kg body weight, orally). All mice were infected intraperitoneally with PbA at a dose of 10^7inocula in 0.2 ml phosphate-buffered saline (PBS) except uninfected group [19, 20]. The parasites were allowed to develop for 48 h, after which treatments were administered on 4 d intervention according to group allocation. On day 7, mice were terminated, liver were harvested for immunohistochemistry preparation [21].

Immunohistochemistry

Mus musculus liver samples were fixed in 10% phosphate-buffered formalin for 24 h, dehydrated through graded ethanol (30–96%), cleared in xylene, and embedded in paraffin. Blocks were sectioned at 5 µm using a Leica microtome, mounted on poly-lysine–coated slides, and incubated at 60 °C for 2 h. Immunohistochemical staining was performed using the DakoEnVision®+Dual Link System-HRP (DAB+). Slides were deparaffinized in xylene, rehydrated through graded ethanol, and rinsed in PBS. Antigen retrieval was conducted in Tris-sodium citrate buffer using a microwave for 15 min at 700 W followed by 15 min at 420 W. After cooling, slides were washed and endogenous peroxidase activity was blocked using 0.3% hydrogen peroxide for 10 min. Slides were incubated with 5% FBS for 10 min, followed by primary antibodies (CAT Polyclonal Antibody, Bioss, USA, Catalog numberbs-2302R, host: Rabbit) 1:100 (diluted with PBS pH 7.4) and incubated for 3 h. After PBS washes, labeled polymer-HRP was applied for 30 min, followed by DAB substrate to visualize positive staining. Sections were counterstained with Meyer's hematoxylin, dehydrated, cleared in xylene, and mounted with Entellan. Images were captured using an Olympus CX41 microscope with an OptilabPro camera at 400× magnification [22]. Quantitative analysis of catalase immunohistochemistry in the liver tissue of malaria-infected mice was performed using ImageJ software (NIH, USA, github. com/imagej/ImageJ). Histopathological images were acquired using an Optilab system and analyzed in JPG format. All images were converted to 8-bit grayscale (Image, Type, 8-bit). DAB-positive areas were segmented using the Adjust Threshold function. Threshold values were empirically determined to distinguish DAB signal from background, with a lower limit of 0 and an upper limit of 140, based on images exhibiting the strongest staining intensity. The same threshold was consistently applied to all images across experimental groups. Quantification included measurement of the percentage of DAB-positive area relative to total tissue area and mean staining intensity, representing catalase immunoreactivity in liver tissue [23]. Data was copied to excel and converted to. spv format.

STATISTICAL ANALYSIS

Data were analysed by Statistical Package for the Social Sciences (SPSS)v27 (IBM, USA).

Data are presented as mean±SD. One-way ANOVA followed by LSD post-hoc tests was used to assess group differences. Statistical significance was set at $p<0.05$.

RESULTS

This study evaluated the interaction of andrographolide compounds, their derivatives, and phase 1 and 2 metabolites with antioxidant enzymes catalase, comparing them with natural ligands and the artemisinin reference compound. As shown in table 2, mean energy binding from docking result, the interaction of ligand and receptor was visualized 2D in BIOVIA and tabulated as type of interaction (hydrophobic and hydrogen bond), amino acid residue. Alkyl, Pi-alkyl, vander walls, Pi-cation, Atractive charge were classified as hydrophobic bond, conventional hydrogen bond and carbon hydrogen bond were classified as hydrogen bond. The minuses energy binding the stronger interaction. Binding energy values (kcal/mol) were obtained from AutoDock4 using the Lamarckian Genetic Algorithm. The predicted inhibition constant (Ki) was calculated automatically by AutoDock4 based on the binding free energy using the thermodynamic equation $\Delta G = RT \ln Ki$. More negative binding energy indicates stronger binding affinity.

The docking results indicate a clear hierarchy of predicted affinities and interaction modes at the catalase active site. The native ligand (−19.98 kcal/mol) binds far more strongly than any tested phytochemicals, implying the active site favors larger or more complementary chemotypes. Among tested compounds, glucuronidated andrographolide metabolites (notably M-3: −9.89 kcal/mol and M-2: −9.51 kcal/mol) show the best binding energies, driven by mixed hydrophobic (alkyl, pi-alkyl, pi-sigma) and multiple polar contacts (Asn148, Val146, Phe334, Tyr358, His75). These extensive interactions likely stabilize the metabolites in the pocket. Non-conjugated andrographolide derivatives (binding energies ranged −6.4 to −7.1 kcal/mol) exhibit moderate affinities; interactions are dominated by contacts with residues Tyr358, Gly147, His75, and Ala133, suggesting engagement near the same entrance/loop region. Artemisinin (−7.11 kcal/mol) and several parent diterpenoids form show weaker or transient binding. Notably, 3-oxoandrographolide and some glucuronides form defined hydrogen bonds (Arg 365, Val73, Ala133, Phe132, Gly147), which likely enhance specificity. Overall, glucuronidation appears to improve predicted binding via additional polar interactions and larger contact surface.

Table 2: Docking result of energy binding and type of bond

Receptors	**Catalase**		
Ligand	**Energy binding (kcal/Mol)**	**Hydrophobic bond**	**Hydrogen bond**
Native ligand	-19.98	Phe161, Met350, Pro158, His218, Tyr358, Val146, Arg 354, His75, Phe153	Arg365, Arg72
Artemisinin	-7.11	Ala133, Val146, His75	His75
Andrographolide	-6.86	His75	Asn148, Gly147, Phe132, Ala133, Val73, Val74
Deoxyandrographolide	-7.03	Tyr358	Arg112, Val74, Gly147
Neoandrographolide	-7.09	Gly147, His75, Ala133	Tyr358, Arg72, Arg365, Val146
14 deoxy-11, 12dehydroandrografolid	-6.4	-	His362, Arg365, Asn148
Isoandrographolide	-6.52	Phe334, Arg112	Arg365, Ala133, Gly147, Phe132, Asn148

14-deoxy-12-hydroxy-andrographolide	-6.87	-	Gly147, Ala133, Phe132, Val74, Val73
14-deoxyandrographolide	-5.2	His75	Thr362, Arg365, Asn148, Phe132, Ala133, Gly147
3-oxoandrographolide	-7.0	His 75	Arg 365, Val73, Ala133, Phe132, Gly147
M1	-8.43	Pi-cation his75	Tyr358, arg354, asn148
M2	-9.51	Halogen val74	
M3	-9.89	Akyl arg72, pi-alkyl tyr358, pi-sigma his75	Asn148, val146, Phe334
M4	-8.12	-	Val74, val73, gly147, tyr358
M5	-8.23	Alkyl Ala133, his75, pi-alkyl val146, phe334	Arg365, gly147, asn148, thr361
M6	-8.65	Pi-sigma his75	Asn148
M7	-8.30	Alkyl ala173	Thr361, arg 365

*Strong affinity<-6 kcal/mol. Hydrophobic bond (Van der walls, pi-alkyl, alkyl, pi-cation, pi-sigma, attractive charge), Hydrogen bond (conventional hydrogen bond, carbon hydrogen bond), Abbreviation: Histidine (His), isoleucine (Ile), leucine (Leu), lysine (Lys), methionine (Met), phenylalanine (Phe), threonine (Thr), tryptophan (Trp), and valine (Val), arginine (Arg), cysteine (Cys), tyrosine (Tyr), and glycine (Gly).

Table 3: Prediction of rule of five of each ligand

Ligand	Molecular weight (Da)	LogP	Rotatable bonds (n)	Aceceptors (n)	Donors (n)	Surface area ($Å^2$)
Andrographolide	350.455	1.96	3	5	3	148.934
Artemisinin	282.336	2.39	0	5	0	118.370
14-deoxy-11,12-didehydroandrographolide	332.44.00	2.76	3	4	2	143.450
Deoxyandrographolide	334.456	3.13	4	4	2	144.140
Isoandrographolide	350.455	2.20	2	5	2	148.937
Neoandrographolide	480.598	1.84	7	8	4	201.139
14-deoxy-12-hydroxyandrographolide	350.455	1.96	4	5	3	148.934
3-oxoandrographolide	348.439	2.17	4	5	2	148.302
14-deoxyandrographolide	334.456	2.99	4	4	2	144.140
M1	449.349	-0.80	3	4	3	155.480
M2	320.47	na	2	3	1	na
M3	333.448	3.48	5	4	1	144.140
M4	309.426	2.55	2	4	3	134.054
M5	296.451	3.53	4	2	1	129.950
M6	420.331	3.30	3	3	1	140.125
M7	324.441	4.45	6	4	1	139.755

*Na: not analyse

The Lipinski's Rule of Five (Ro5) prediction (Table.3) indicates that most ligands have molecular weights below 500 Da and acceptable numbers of hydrogen bond donors and acceptors, suggesting moderate potential for oral bioavailability. Many andrographolide compounds and their derivatives exhibit good LogP values, according the Ro5 threshold (LogP ≤ 5), which indicates slight lipophilicity and potential limitations in solubility and intestinal absorption. Neoandrographolide presents additional Ro5 violations due to its higher molecular weight and increased number of rotatable bonds. In contrast, several metabolites (M1–M4) display more balanced Ro5 profiles, suggesting comparatively improved pharmacokinetic properties relative to the parent compounds.

Molecular dynamic analyses reveal (fig. 1) catalase–artemisinin (green) exhibits an RMSD profile that reaches equilibrium rapidly during the early phase of the simulation, followed by relatively small fluctuations after stabilization. This indicates that artemisinin interacts with the active pocket of catalase in a stable manner without inducing major alterations in the overall protein conformation. Catalase–andrographolide (Blue) shows higher RMSD values with larger fluctuations throughout the simulation, suggesting that andrographolide binding triggers secondary-structure reorganization during the initial phase before achieving a new equilibrium. These patterns reflect that the catalase–artemisinin complex is more conformationally stable, whereas andrographolide induces adaptive structural adjustments indicative of stronger or more flexible interactions with the active site. Lower RMSD stability in the artemisinin complex implies a non-disruptive inhibitory mechanism, whereas higher RMSD in the andrographolide complex suggests stronger binding or induction of conformational changes. The catalase–artemisinin complex displays low RMSF values across most domains, especially within the active region; only a few surface residues exhibit slight increases, indicating that artemisinin maintains structural rigidity. In contrast, catalase–andrographolide shows increased RMSF in residues surrounding the active site and flexible loop regions, suggesting enhanced local dynamics, likely driven by altered intramolecular hydrogen bonding or more dynamic hydrophobic interactions.

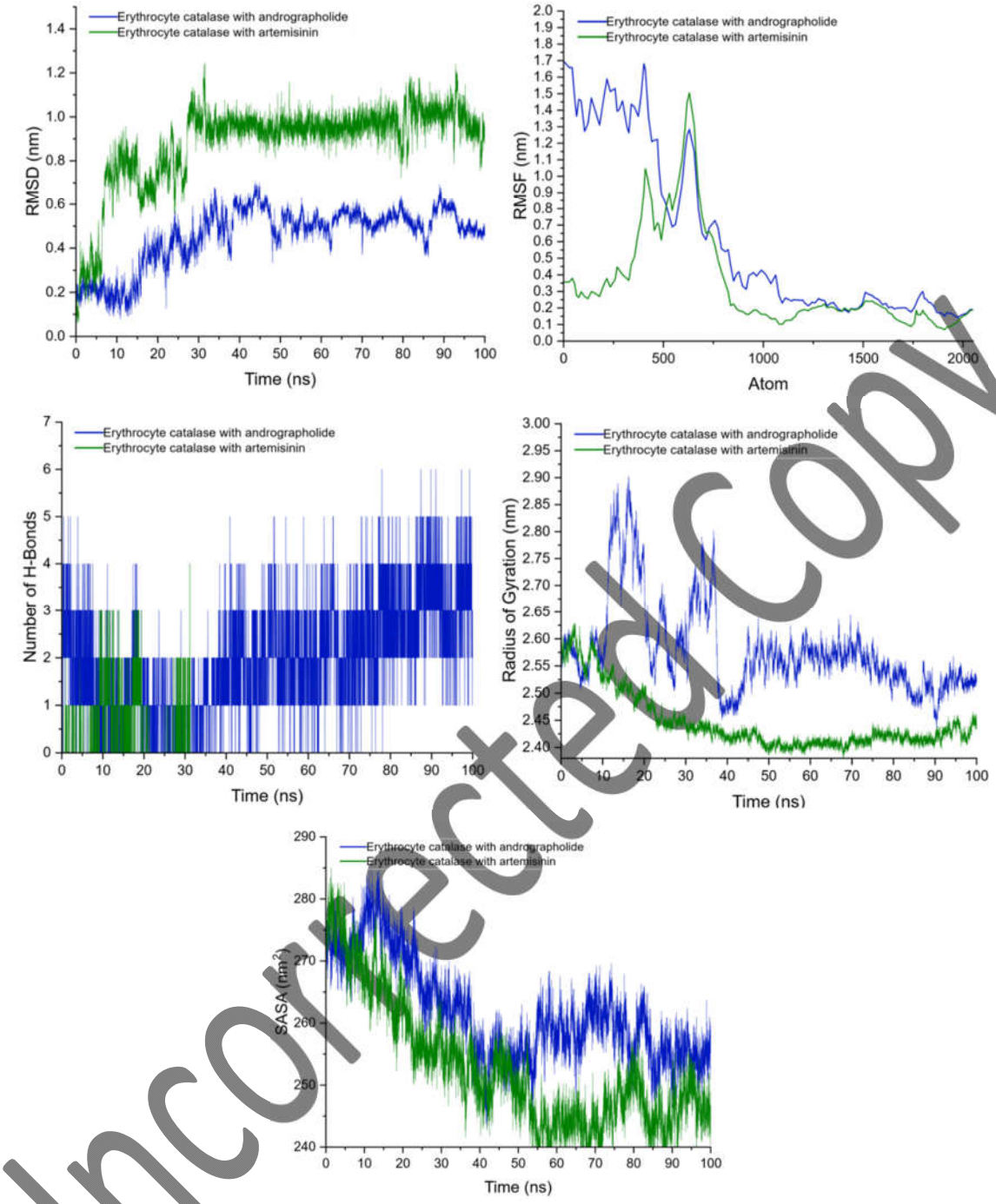

Fig. 1: Molecular dynamic interaction of IDGF with Andrographolide compared with Artemisinin with 5 parameter RMSD, RMSF, H-bond, Rg, SASA

Elevated RMSF in the andrographolide complex reflects active-site residue adjustments to optimize ligand interactions, whereas the low RMSF in the artemisinin complex suggests a more static stabilizing effect. Hydrogen bonding analysis shows that catalase–artemisinin forms relatively few, fluctuating H-bonds (0–3), indicating weak and transient interactions with active-site residues. Catalase–andrographolide, however, exhibits a much higher and more consistent number of H-bonds (3–6), demonstrating stronger affinity and a more persistent complex. The hydroxyl and lactone groups in andrographolide enable extensive hydrogen bond networks with polar residues such as His, Ser, or Tyr, supporting its role as a more effective inhibitor of catalase's oxidative activity. Radius of gyration (Rg) results show that catalase–artemisinin maintains a low and stable Rg (2.4–2.5 nm), indicating preserved protein compactness. Catalase–andrographolide shows slightly higher Rg values (2.6–2.7 nm) with early fluctuations, indicating partial relaxation or expansion of the protein due to strong ligand interactions, but later stabilizes, reflecting a compact yet adapted equilibrium state. Solvent accessible surface area analysis reveals that catalase–artemisinin gradually decreases solvent exposure, enhancing protein compactness. Catalase–andrographolide starts with higher SASA and prolonged fluctuations, indicating initial surface residue rearrangements before reaching a new equilibrium. The catalase–andrographolide complex undergoes dynamic conformational transitions that transiently increase solvent exposure but ultimately form a tightly bound and stable complex.

Immunohytochemistry

The negative control group exhibited the highest staining intensity with a wide distribution indicating pronounced and heterogeneous antigen expression under untreated pathological conditions. Artesunate monotherapy markedly reduced staining intensity, yielding values comparable to the normal control, which suggests effective suppression of target antigen expression. Treatment with andrographolide resulted in a moderate reduction in staining intensity, lower than the negative control but higher than both the artesunate and normal control groups, indicating a partial inhibitory effect. Notably, the combination of andrographolide and artesunate produced the lowest staining intensity, even below normal control levels, supporting a synergistic interaction in suppressing antigen expression.

Table 2: Intensity and percent area of catalase expression comparation between group

Variable	N	Mean±SD	95% CI		Min	Max
			Lower	Upper		
Intensity						
Negative	5	3.04±2.38	0.08	5.99	0.00	6.39
Artesunat	5	0.09±0.07	0.01	0.18	0.00	0.18
Andrographolid	5	1.01±0.67	0.18	1.84	0.30	1.81
Combination	5	0.01±0.03	-0.02	0.04	0.00	0.06
Normal Control	5	0.04±0.06	-0.03	0.11	0.00	0.11
Total	25	0.84±1.56	0.20	1.48	0.00	6.39
Percent area						
Negative	5	1.19±0.93	0.03	2.35	0.00	2.51
Artesunat	5	0.04±0.03	0.00	0.07	0.00	0.07
Andrographolid	5	0.40±0.26	0.07	0.72	0.12	0.71
Combination	5	0.00±0.01	-0.01	0.02	0.00	0.02
Normal control	5	0.02±0.03	-0.02	0.06	0.00	0.06
Total	25	0.33±0.61	0.08	0.58	0.00	2.51

A similar pattern was observed in the percentage of positive area. The negative control exhibited the highest immunoreactive area, reflecting extensive antigen distribution within the tissue. Artesunate therapy significantly reduced the positive area, whereas andrographolide treatment produced a moderate reduction. Consistently, the combination group showed the lowest percentage of positive area, comparable to the normal control, indicating normalization of antigen expression and tissue distribution.

Table 3: Pos hoc LSD comparation between group

Group	Mean difference (MD)	p-value	95% CI	
			Lower	Upper
Negative-Artesunat	2.94	0.001***	1.48	4.40
Negative-Andrographolide	2.02	0.009**	0.56	3.48
Negative-Combination	3.02	0.001***	1.56	4.48
Negative-Normal	2.99	0.001***	1.53	4.45
Andrographolide-Negative	-2.03	0.009**	-3.48	-0.56
Combination-Negative	-3.02	0.001***	-4.48	-1.56
Normal-Negative	-2.99	0.001***	-4.45	-1.53
Negative-Artesunate	1.15	0.001***	0.580	1.72
Negative-Andrographolide	0.79	0.009**	0.22	1.36
Negative-Combination	1.18	0.001***	0.61	1.75
Negative-Normal	1.16	0.001***	0.59	1.74
Artesunate-Negative	-1.15	0.001***	-1.72	-0.58
Andrographolide-Negative	-0.79	0.009**	-1.36	-0.22
Combination-Negative	-1.19	0.001***	-1.76	-0.61
Normal-Negative	-1.17	0.001***	-1.74	-0.59

*p<0.05, ** p<0.01, ***p<0.001

As shown in table 3, multiple comparison analysis revealed that the negative control group differed significantly from all treatment groups and the normal control (p<0.01). Positive mean differences in the Negative–Artesunate, Negative–Andrographolide, Negative–Combination, and Negative–Normal comparisons indicate that the measured parameter was consistently higher in the negative control than in the other groups. The Negative–Combination comparison showed the largest mean difference, both in the first analysis set (MD = 3.03; 95% CI: 1.57–4.49) and in the second set (MD = 1.19; 95% CI: 0.61–1.76), indicating that combination therapy produced the strongest reduction compared with the untreated condition. Conversely, reciprocal comparisons (Artesunate–Negative, Andrographolide–Negative, Combination–Negative, and Normal–Negative) yielded significant negative mean differences, confirming a substantial reduction due to the interventions. Overall, these findings demonstrate that all treatments significantly decreased the measured parameter, with the greatest effect observed in the combination group, approaching normal control levels.

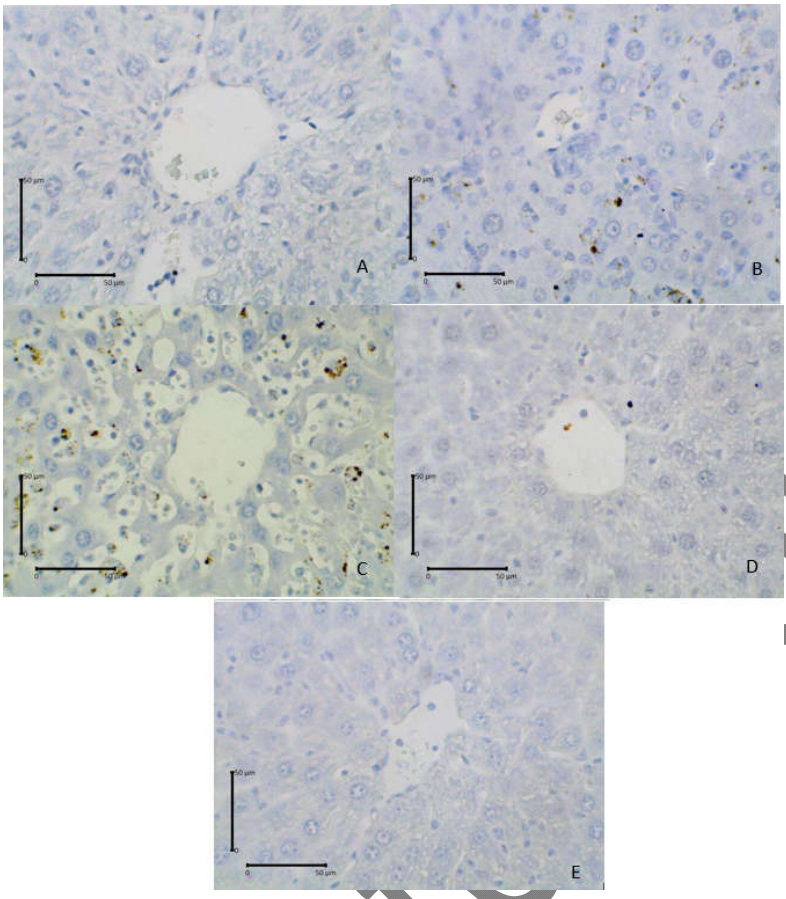

Fig. 2: Catalase expression by IHC reveal A (Arsesunate), B (Andrographolide), C (Negative control), D (Combination), E (Normal control)

The expression of catalase exhibited a pattern strongly influenced by parasitemia levels and treatment type. In the untreated negative group (fig. 2C) show high expression of catalase for balancing oxidative stress produced by high invaded hepatocyte by parasite. This condition stimulated cells to maximally upregulate catalase expression as a compensatory mechanism to neutralize the accumulation of free radicals, particularly hydrogen peroxide. In the Artesunate-treated group (fig. 2A), catalase expression appeared weak. Although Artesunate effectively reduced parasitemia, the drug acts through the generation of free radicals to eliminate the pathogen so invaded erythrocyte must be decreased. Fig. 2B show administration of andrographolide resulted in a moderate level of catalase expression. This compound possesses antioxidant and immunomodulatory properties, enabling it to reduce parasitemia while simultaneously stimulating the upregulation of cellular defense enzymes, but not totally eradicated infected hepatocyte resulting in moderate catalase expression to balance stress oxydative. In the combination group receiving both artesunate and andrographolide (fig. 2D), catalase levels were reduced to values indistinguishable from uninfected (fig. 2E, normal controls). This may indicate an antagonistic interaction that suppresses the enzymatic antioxidant pathway or reduces parasite number directly so decreased the cellular requirement for catalase compensation.

DISCUSSION

This study represents an initial breakthrough that comprehensively explores the potential of andrographolide, especially isoandrographolide-19-O-beta-D-glucuronide (M-2), 14-deoxy-12-hydroxyandrographolide-19-O-beta-D-glucuronide (M-3), in targeting human erythrocyte catalase, these data indicate that despite undergoing biotransformation through phase I, such as oxidation and reduction and phase II conjugation processes, the resulting metabolites retain and, in some cases, even enhance their affinity for target proteins. These metabolites tend to be more polar and hydrophilic, thereby overcoming the lipophilic solubility limitations of the original andrographolide and enabling broader distribution within biological systems [9].

In the context of malaria pathophysiology, oxidative stress triggered by erythrocyte lysis and heme release, as well as the Fenton reaction plays an important role in exacerbating tissue damage. Andrographolide has been shown to act as a multitarget agent by activating the endogenous antioxidant system through increased activity of SOD and catalase, effectively neutralizing these free radicals. This finding aligns with previous studies demonstrating the antioxidant effects of andrographolide in other disease models such as atherosclerosis, confirming the redox-modulating capacity of this compound across pathological conditions [24].

Molecular dynamics simulations revealed that andrographolide exhibited stronger interactions and greater stabilization of the 1DGF protein compared with artemisinin, suggesting its potential as an adjuvant therapy to help overcome *Plasmodium* resistance [25,26]. In contrast to the present study, previous research using a methanolic extract of *Andrographis paniculata* leaves (1 g/kg body weight) in a carbon tetrachloride (CCl_4)-induced oxidative stress rat model did not show a significant alteration ($p>0.05$) in plasma total antioxidant status compared with the control group. Under normal physiological conditions, andrographolide has been reported to enhance antioxidant defense by increasing the activity of several antioxidant enzymes, including glutamate–cysteine ligase (GCL) catalytic and modifier subunits, superoxide dismutase (SOD)-1, heme oxygenase (HO)-1, and glutathione S-transferase (GST) in rats [27]. In a rheumatoid arthritis rat model, treatment with andrographolide increased the levels of antioxidant enzymes, including superoxide dismutase, catalase, and glutathione [28]. In contrast to this research, Bo Li *et al.* demonstrated that *Andrographis paniculata* at concentrations of 0.625 µg/ml and 2.5 µg/ml attenuated oxidative stress–induced injury in chondrocytes by enhancing cell proliferation

suppressed by H_2O_2 and by increasing antioxidant enzyme activities, including SOD and catalase [29]. Another study further confirmed the *in vitro* antioxidant potential of andrographolide through its free radical scavenging activity. Co-administration of andrographolide significantly reduced toxicant-induced hepatic damage. The toxicant exposure resulted in a decline in endogenous hepatic antioxidant enzymes, such as catalase, superoxide dismutase, and glutathione; however, andrographolide treatment restored their levels. In breast cancer stem cells (BCSCs), andrographolide modulate manganese superoxide dismutase (MnSOD) activity but not catalase [30].

An important mechanism of the antioxidant system involves not only changes in enzyme activity but also the maintenance of redox balance between reduction and oxidation reactions. In the context of infectious diseases and pathogen elimination, the production of oxidative stress plays a crucial role as a host defense mechanism against pathogen invasion [31]. Reactive oxygen species are generated to damage pathogen lipid membranes and to induce denaturation or alkylation of pathogen DNA or RNA. The critical factor is the maintenance of an appropriate balance between oxidative and reductive processes [32]. Under conditions of oxidative stress, cells upregulate the expression of antioxidant enzymes such as catalase through activation of redox-sensitive transcription factors (nuclear factor erythroid 2–related factor 2 (Nrf2), forkhead box O (FoxO), and activator protein-1 (AP-1) and chromatin remodeling, resulting in elevated catalase levels when ROS/H_2O_2 burden is high [32, 33]. When combination therapy with andrographolide–artesunate effectively reduces ROS, the upstream signals that induce these pathways are attenuated; consequently, the catalase promoter returns to a basal state through suppression of activating factors and/or reinforcement of repressive factors, leading to a decline in catalase expression toward normal levels, even though andrographolide may still be structurally capable of binding to the enzyme. This pattern of "catalase overexpression during stress followed by normalization as stress resolves" has been widely reported across various models of oxidative stress and cellular adaptation [34].

ROS levels are suppressed to the physiological range, the availability of ROS as signaling molecules required to sustain high catalase expression diminishes, eliminating the selective pressure to maintain elevated catalase levels. In this context, andrographolide binding to catalase is more likely to modulate enzyme activity or stability at physiological expression levels rather than drive further upregulation [35]. The observed decrease in catalase expression toward normal levels in the combination treatment group can therefore be interpreted as a reflection of restored redox homeostasis through negative feedback regulation of antioxidant pathways following successful ROS reduction, consistent with docking results indicating strong inhibitory interactions with the catalase enzyme.

Multiple studies have demonstrated that high-affinity ligands interacting with catalase can act as inhibitors through structural mechanisms. Ligand binding may induce conformational changes in the protein, including a reduction in α-helical content and alterations in secondary structure, which impair catalytic activity even without directly disrupting the heme active site [36]. In addition, ligands may bind to non-active regions, such as allosteric sites or domain interfaces, thereby perturbing the structural dynamics surrounding the active site and reducing enzymatic efficiency. Previous study show 4-chlorophenol has been reported to bind within a cavity between the helical domain and the threading arm of catalase via van der Waals interactions and hydrogen bonding, leading to loss of α-helical structure and decreased catalytic activity [37]. Similarly, benzo-a-pyrene exhibits high docking affinity (approximately−11.2 kcal/mol) near the catalase active site and induces conformational changes associated with reduced catalase activity at both cellular and purified protein levels [38]. These findings underscore that high binding affinity frequently correlates with enzyme inhibition when the bindinglocation and structural consequences disrupt the enzyme's optimal conformation. Furthermore, reductions in intracellular catalase activity may arise from direct enzymatic inhibition by tightly bound ligands as well as from alterations in the cellular redox environment [39]. Changes in reactive oxygen species (ROS) levels can modulate catalase stability and promote post-translational modifications that diminish enzymatic activity or accelerate protein degradation. In contrast, catalase expression at the mRNA and protein levels is regulated by transcriptional pathways, such as Nrf2 signaling, whichcannot be predicted by docking approaches alone [40].

Therefore, in silico binding affinity predictions are generally effective for ranking ligands based on interaction strength but are insufficient for reliably inferring functional outcomes (activation versus inhibition) without complementary data on protein conformation and molecular dynamics. Docking models are typically trained on affinity datasets rather than on downstream biological consequences, such as changes in geneexpression, signaling pathways, or protein turnover [41]. Consequently, the apparent paradox between in silico predictions and experimental observations arises because these approaches address fundamentally different questions: docking evaluates how strongly a ligand binds to a protein, whereas *in vitro* and *in vivo* experiments determine what happens to enzyme function and cellular responses after ligand binding.

CONCLUSION

Andrographolide exhibits potent antimalarial and antioxidant activities, primarily through electron-scavenging mechanisms that reduce oxidative stress during hepatic malaria. The reduction in oxidative stress, together with effective pathogen elimination, may lead to a decreased requirement for catalase activity. Nevertheless, further research is required to evaluate the clinical efficacy in catalase expression and therapeutic potential of andrographolide in patients with malaria.

ACKNOWLEDGEMENT

During the preparation of this work, the author used DeepL for language polishing and gmar correction. After using this tool, the authors reviewed and edited the content as needed and take full responsibility for the content of the publication.

FUNDING

Nil

AUTHORS CONTRIBUTIONS

P. I. B. A: Conceptualisation, designed, sample collection, performed *in vivo* experiments, data interpretation, and manuscript writing. D. A. A. S. L: Performed *in vivo*, data interpretation and supported in manuscript writing. B. K. S: Performed in silico experiments and manuscript writing. I. K. S concepting and reviewing manuscript, D. K. W proofreading manuscript, I. M. A. G. W: Conceptualisation, designed, supervision, reviewed and edited the manuscript.

CONFLICT OF INTERESTS

Declared none

REFERENCES

1. World Health Organization. https://www. who. int/news-room/fact-sheets/detail/malaria. Malaria;2. World Health Organization. https://www. who. int/southeastasia/health-topics/malaria. Accessed 2 January 2026. 2024. Malaria in South East Asia.

2. World Health Organization. Malaria: artemisinin partial resistance [Internet]. In: https://www. Google.com/url?sa=tandsource=webandrct=jandopi=89978449andurl=https://www. who. int/news-room/questions-and-answers/item/artemisinin-resistanceand. [cited 2026 Jan 31] [report]. Available.
3. Dharmasamitha I, Mas Rusyati LM, Wati DK, Gelgel Wirasuta IM. The potential anti-psoriatic effects of andrographolide: A comparative study to topical corticosteroids. Recent Adv Inflamm Allergy Drug Discov. 2025;19(1):46-70. doi: 10.2174/0127722708296983240424102212, PMID 38712377.
4. Ibraheem ZO, Majid RA, Sidek HM, Noor SM, Yam MF, Abd Rachman Isnadi MF et al. *In vitro* antiplasmodium and chloroquine resistance reversal effects of andrographolide. Evid Based Complement Alternat Med. 2019;2019:7967980. doi: 10.1155/2019/7967980, PMID 31915453.
5. Putra AM, Chaidir HM, Hanafi M, Pan Y, Yanuar A. Andrographolide and its derivative-A story of antimalarial drug design and synthesis. Int J Appl Pharm. 2017 Oct 1;9:98-101. doi: 10.22159/ijap.2017.v9s1.55_61.
6. Dixit N, Motwani H, Patel SK, Rawal RM, Solanki HA. Decoding the mechanism of andrographolide to combat hepatocellular carcinoma: a network pharmacology integrated molecular docking and dynamics approach. J Biomol Struct Dyn. 2024 Dec 2;42(19):10237-55. doi: 10.1080/07391102.2023.2256866, PMID 37728545.
7. Citra SN, Arfan A, Alroem A, Bande LS, Irnawati I, Arba M. Docking-based workflow and ADME prediction of some compounds in Curcuma longa and Andrographis paniculata as polymerase PA-PB1 inhibitors of influenza A/H5N1 virus. J Res Pharm. 2023;27(1):221-31.
8. Cui L, Qiu F, Yao X. Isolation and identification of seven glucuronide conjugates of andrographolide in human urine. Drug Metab Dispos. 2005 Apr;33(4):555-62. doi: 10.1124/dmd.104.001958, PMID 15644451.
9. Terefe EM, Ghosh A. Molecular Docking, Validation, Dynamics Simulations, and pharmacokinetic Prediction of Phytochemicals Isolated from Croton dichogamus against the HIV-1 reverse transcriptase. Bioinform Biol Insights. 2022;16:11779322221125605. doi: 10.1177/11779322221125605, PMID 36185760.
10. Veerasamy R, Karunakaran R. Molecular docking unveils the potential of andrographolide derivatives against COVID-19: an in silico approach. J Genet Eng Biotechnol. 2022 Dec;20(1):58. doi: 10.1186/s43141-022-00339-y, PMID 35420322.
11. Yasir M, Park J, Han ET, Park WS, Han JH, Kwon YS et al. Computational exploration of licorice for lead compounds against Plasmodium vivax Duffy Binding protein utilizing molecular docking and molecular dynamic simulation. Molecules. 2023 Apr 1;28(8):3358. doi: 10.3390/molecules28083358, PMID 37110591.
12. Hudiyanti D, Khairiah R, Siahaan P, Majid FA, Fachriyah E, Zakaria NH. Enhanced stability and binding efficiency of liposomal andrographolide complexes targeting human papillomavirus for cervical cancer therapy: molecular docking and molecular dynamics simulations. Results Chem. 2025 Jul;16:102342. doi: 10.1016/j.rechem.2025.102342.
13. Megantara S, Fauzan MA, Saputri FA, Ferdiansyah Sofian F. Journal of Global Pharma Technology Pharmacophore Screening and Molecular Docking of Andrographolide and Its Derivatives on Plasmepsin as Anti-Malarial Drug [Internet] [report]. org/Pdb. [cited 2026 Mar 21]. Available from: http://www.rcsb.
14. Warditiani NK, Susanti NM, Arisanti CI, Putri NP, Wirasuta IM. Antidyslipidemia and antioxidant activity of andrographolide compound from Sambiloto (Andrographis paniculata) herb. Int J Pharm Pharm Sci. 2017 Jul 1;9(7):59. doi: 10.22159/ijpps.2017v9i7.18109.
15. Rokkam SK, Bhujel M, Jain D, Sripada L, Nanduri S, Bajaj A et al. Synthesis of novel pyrazole acetals of andrographolide and isoandrographolide as potent anticancer agents. RSC Adv. 2024;14(36):26625-36. doi: 10.1039/D4RA00547C, PMID 39175689.
16. Kasemsuk T, Piyachaturawat P, Bunthawong R, Sirion U, Suksen K, Suksamrarn A et al. One-pot three steps cascade synthesis of novel isoandrographolide analogues and their cytotoxic activity. Eur J Med Chem. 2017 Sep;138:952-63. doi: 10.1016/j.ejmech.2017.07.035, PMID 28755636.
17. Budiapsari PI, Jaya PK, Dewi PM, Laksemi DA, Horng JT. Effect of moringa extract on parasitemia, monocyte activation and organomegaly among Mus musculus infected by Plasmodium berghei ANKA. Narra J. 2024 Mar 19;4(1):e653. doi: 10.52225/narra.v4i1.653, PMID 38798832.
18. Laksemi DA, TK; ADPA, SIM, WIPE D, LNM. Evaluation of antimalarial activity of combination extract of Citrus aurantifolia and honey against Plasmodium berghei–infected mice. Trop J Nat Prod Res. 2023 Feb 1;7(1).
19. Khrisna P, Jaya D, Indah P, Apsari B, Made P, Putri AC et al. Effects of Moringa Oleifera extract as an immunomodulator of lymphocyte cells and macrophages in BALB/c mice infected with Plasmodium berghei. Folia Med Indones. 2023;59(3).
20. Arwati H, Bahalwan RR, Hapsari WT, Wardhani KA, Aini KN, Apsari PI et al. Suppressive effect of goat bile in Plasmodium berghei ANKA infection in mice. Vet World. 2021 Aug 1;14(8):2016-22. doi: 10.14202/vetworld.2021.2016-2022, PMID 34566316.
21. Adnyaswari DA, Indrayani AW, Artini IgA, Ernawati DK, Trapika IGMGSC, Sriwidyani NP, Arijana IGKN. Immunohistochemical Analysis of Tumor Suppressor p53 in p-Dimethylamino Benzaldehyde (DMBA) Induced Hepatocarcinogenesis in Rats (Rattus norvegicus L.) Male Wistar Strains. Journal of Cancer and Tumor International. 2024 Oct 17;14(4):73–83.
22. Crowe AR, Yue W. Semi-quantitative determination of protein expression using immunohistochemistry staining and analysis: an integrated protocol. Bio Protoc. 2019;9(24):e3465. doi: 10.21769/BioProtoc.3465, PMID 31867411.
23. Baru Venkata R, Prasanth DS, Pasala PK, Panda SP, Tatipamula VB, Mulukuri S et al. Utilizing Andrographis paniculata leaves and roots by effective usage of the bioactive andrographolide and its nanodelivery: investigation of antikindling and antioxidant activities through in silico and *in vivo* studies. Front Nutr. 2023;10:1185236. doi: 10.3389/fnut.2023.1185236, PMID 37324729.
24. Bhattarai A, Priyadharshini A, Emerson IA. Investigating the binding affinity of andrographolide against human SARS-CoV-2 spike receptor-binding domain through docking and molecular dynamics simulations. J Biomol Struct Dyn. 2023 Dec 29;41(22):13438-53. doi: 10.1080/07391102.2023.2174596, PMID 36764825.
25. Sungthong B, Winyupan S, Nunthaboot N, Phimarn W, Sripadung P. A novel green extraction and molecular docking study: effect of native cyclodextrins and derivatives on the extraction of andrographolide from Andrographis paniculata (Burm.f.) Nees. Trop J Nat Prod Res. 2023 Oct 29;7(10):4262-6.
26. Akowuah GA, Zhari I, Mariam A, Yam MF. Absorption of andrographolides from Andrographis paniculata and its effect on CCl(4)-induced oxidative stress in rats. Food Chem Toxicol. 2009 Sep;47(9):2321-6. doi: 10.1016/j.fct.2009.06.022, PMID 19540299.
27. Li X, Yuan K, Zhu Q, Lu Q, Jiang H, Zhu M et al. Andrographolide ameliorates rheumatoid arthritis by regulating the apoptosis–NETosis balance of neutrophils. Int J Mol Sci. 2019 Oct 2;20(20):5035. doi: 10.3390/ijms20205035, PMID 31614480.
28. Li B, Jiang T, Liu H, Miao Z, Fang D, Zheng L et al. Andrographolide protects chondrocytes from oxidative stress injury by activation of the Keap1-Nrf2-Are signaling pathway. J Cell Physiol. 2018;234(1):561-71. doi: 10.1002/jcp.26769, PMID 30071128.
29. Rachman AT, Suraduhita A, Syahrani RA, Louisa M, Wanandi SI. Suppression of MnSOD by andrographolide and its relation to oxidative stress and viability of breast cancer stem cells treated with repeated doxorubicin administration. In: Proceedings of the 1st Jenderal soedirman international medical conference in conjunction with the 5th Annual Scientific Meeting (Temilnas) Consortium of Biomedical Science Indonesia. SCITEPRESS-Science and Technology Publications; 2020. p. 28-34. doi: 10.5220/0010487200280034.
30. He L, He T, Farrar S, Ji L, Liu T, Ma X. Antioxidants maintain cellular redox homeostasis by elimination of reactive oxygen species. Cell Physiol Biochem. 2017;44(2):532-53. doi: 10.1159/000485089, PMID 29145191.
31. Gallorini M, Petzel C, Bolay C, Hiller KA, Cataldi A, Buchalla W et al. Activation of the Nrf2-regulated antioxidant cell response inhibits HEMA-induced oxidative stress and supports cell viability. Biomaterials. 2015 Jul;56:114-28. doi: 10.1016/j.biomaterials.2015.03.047, PMID 25934285.

32. Glorieux C, Calderon PB. Catalase down-regulation in cancer cells exposed to arsenic trioxide is involved in their increased sensitivity to a pro-oxidant treatment. Cancer Cell Int. 2018 Dec 20;18(1):24. doi: 10.1186/s12935-018-0524-0, PMID 29467594.
33. Glorieux C, Zamocky M, Sandoval JM, Verrax J, Calderon PB. Regulation of catalase expression in healthy and cancerous cells. Free Radic Biol Med. 2015 Oct;87:84-97. doi: 10.1016/j.freeradbiomed.2015.06.017, PMID 26117330.
34. Li B, Ming H, Qin S, Nice EC, Dong J, Du Z et al. Redox regulation: mechanisms, biology and therapeutic targets in diseases. Signal Transduct Target Ther. 2025 Mar 7;10(1):72. doi: 10.1038/s41392-024-02095-6, PMID 40050273.
35. Kribelbauer JF, Rastogi C, Bussemaker HJ, Mann RS. Low-affinity binding sites and the transcription factor specificity paradox in eukaryotes. Annu Rev Cell Dev Biol. 2019;35:357-79. doi: 10.1146/annurev-cellbio-100617-062719, PMID 31283382.
36. Wang J, Yu X, Jia R, Liu R, Zong W. An *in vitro* and in silico study to explore the response of catalase to 4-chlorophenol and their interacting mechanisms. J Mol Liq. 2021;337:116444. doi: 10.1016/j.molliq.2021.116444.
37. Jena AB, Rath S, Subudhi U, Dandapat J. Molecular interaction of benzo-a-pyrene inhibits the catalytic activity of catalase: insights from biophysical and computational studies. J Mol Struct. 2022;1265:133494. doi: 10.1016/j.molstruc.2022.133494.
38. Bell DR, Weber JK, Yin W, Huynh T, Duan W, Zhou R. In silico design and validation of high-affinity RNA aptamers targeting epithelial cellular adhesion molecule dimers. Proc Natl Acad Sci U S A. 2020;117(15):8486-93. doi: 10.1073/pnas.1913242117, PMID 32234785.
39. Tare H, Thube U, Kachave R, Wagh V, Udugade B. Catechins as catalase modulators: A comprehensive in-silico analysis unveiling their potential antioxidant effects. Int J Drug Deliv Technol. 2023;13(4):1156-60. doi: 10.25258/ijddt.13.4.05.
40. Uluçay T, Arslan M, Döşeme H, Kalyoncu S, Kale S. Toward accurate in silico prediction of antigen binding affinities for antibody engineering. Adv Protein Chem Struct Biol. 2025;147:21-35. doi: 10.1016/bs.apcsb.2024.11.006, PMID 40973400.